

# Singlet-Doublet Transitions of a Quantum Dot Josephson Junction Detected in a Transmon Circuit

Arno Bargerbos<sup>1,\*;†</sup>, Marta Pita-Vidal<sup>1,‡</sup>, Rok Žitko,<sup>2,3</sup> Jesús Ávila,<sup>4</sup> Lukas J. Splitthoff,<sup>1</sup> Lukas Grünhaupt,<sup>1</sup> Jaap J. Wessdorp,<sup>1</sup> Christian K. Andersen<sup>1</sup>, Yu Liu<sup>5</sup>, Leo P. Kouwenhoven,<sup>1</sup> Ramón Aguado,<sup>4</sup> Angela Kou,<sup>6</sup> and Bernard van Heck<sup>1,7</sup>

<sup>1</sup> QuTech and Kavli Institute of Nanoscience, Delft University of Technology, Delft 2600 GA, Netherlands

<sup>2</sup> Jožef Stefan Institute, Jamova 39, Ljubljana SI-1000, Slovenia

<sup>3</sup> Faculty of Mathematics and Physics, University of Ljubljana, Jadranska 19, Ljubljana SI-1000, Slovenia

<sup>4</sup> Instituto de Ciencia de Materiales de Madrid (ICMM), Consejo Superior de Investigaciones Científicas (CSIC), Sor Juana Ines de la Cruz 3, Madrid 28049, Spain

<sup>5</sup> Center for Quantum Devices, Niels Bohr Institute, University of Copenhagen, Copenhagen 2100, Denmark

<sup>6</sup> Department of Physics and Frederick Seitz Materials Research Laboratory, University of Illinois Urbana-Champaign, Urbana, Illinois 61801, USA

<sup>7</sup> Leiden Institute of Physics, Leiden University, Niels Bohrweg 2, Leiden 2333 CA, Netherlands

(Received 28 February 2022; revised 23 May 2022; accepted 24 May 2022; published 21 July 2022)

We realize a hybrid superconductor-semiconductor transmon device in which the Josephson effect is controlled by a gate-defined quantum dot in an InAs-Al nanowire. Microwave spectroscopy of the transition spectrum of the transmon allows us to probe the ground-state parity of the quantum dot as a function of the gate voltages, the external magnetic flux, and the magnetic field applied parallel to the nanowire. The measured parity phase diagram is in agreement with that predicted by a single-impurity Anderson model with superconducting leads. Through continuous-time monitoring of the circuit, we furthermore resolve the quasiparticle dynamics of the quantum dot Josephson junction across the phase boundaries. Our results can facilitate the realization of semiconductor-based  $0\text{-}\pi$  qubits and Andreev qubits.

DOI: 10.1103/PRXQuantum.3.030311

## I. INTRODUCTION

Superconducting pairing and charging energy are two fundamental interactions that determine the behavior of mesoscopic devices. Notably, when a quantum dot (QD) is coupled to a superconductor, they compete to determine its ground state. A large charging energy favors single-electron doublet occupancy of the dot and thus a spin-1/2 ground state, while a strong coupling to the superconducting leads favors double occupancy in a singlet configuration with zero spin. A quantum phase transition between the singlet and doublet ground state can occur as system parameters such as the dot energy level and the

coupling strength are varied. The latter also controls the nature of the singlet ground state, which can be of either the Bardeen-Cooper-Schrieffer (BCS) type or the Kondo type. The rich phase diagram of the system, as well as its transport properties, are theoretically well captured by an Anderson model with superconducting leads [1–10].

Quantum dots coupled to superconductors have been studied experimentally over the past two decades. Signatures of the singlet-doublet transition have been detected in tunneling spectroscopy measurements of  $N$ -QD- $S$  devices (where  $N$  is a normal lead, and  $S$  is a superconducting one) via the observation of Fermi-level crossings [11–19]. Additionally, they have been detected in switching-current measurements of  $S$ -QD- $S$  devices via  $\pi$  phase shifts in the current-phase relation of the resulting quantum dot Josephson junction [19–31].

Recent experiments [32–34] on Andreev-pair and spin qubits [35–38] have renewed the interest in quantum dot junctions due to the possibility of tuning the ground state of the system to be in addressable spin states. Knowledge of the phase diagram of the quantum dot junction is also

\*a.bargerbos@tudelft.nl

†These two authors contributed equally.

Published by the American Physical Society under the terms of the [Creative Commons Attribution 4.0 International license](#). Further distribution of this work must maintain attribution to the author(s) and the published article's title, journal citation, and DOI.

beneficial for realizing proposals for a quantum-dot-based readout of topological qubits [39–41].

These developments have highlighted the need for a better fundamental understanding of the quantum dot junction and its dynamics, requiring tools that are not limited by the long integration times of low-frequency measurements or by the invasiveness of transport probes. To address this need, we embed a fully controllable quantum dot in a microwave superconducting circuit. This experimental choice is motivated by the success of circuit quantum electrodynamics (QED) techniques in the investigation of mesoscopic effects in Josephson junctions [32–34,42–49], which stems from its enhanced energy and time resolution compared to low-frequency transport techniques. In this context, the microwave response of a quantum dot junction has attracted recent theoretical [50,51] and experimental [52] attention.

The core of our experiment is a transmon circuit formed by an island with charging energy  $E_c$ , coupled to ground via a superconducting quantum interference device (SQUID) formed by a parallel combination of a junction with a known Josephson energy  $E_J$  and a quantum dot junction [Figs. 1(a)–1(c)]. The energy-phase relation of the quantum dot junction depends on whether it is in a singlet or doublet state, with a characteristic  $\pi$  phase shift between the two relations [Fig. 1(d)] [53]. The two energy-phase relations of the junctions add up together in the SQUID. Depending on whether the quantum dot junction is in the singlet or doublet state, as well as on the external flux, this results in a higher or lower curvature of the total potential around its minimum with respect to that of the reference junction. Therefore, the two branches of the spectrum give rise to two distinct transition frequencies of the transmon circuit, which can be detected and distinguished via standard circuit-QED techniques [54]. As a result, a transition from a singlet to a doublet state will appear as a discontinuous jump in a measurement of the transmon frequency spectrum.

Using this method, we detect the singlet-doublet transition and reconstruct the phase diagram of a quantum dot junction as a function of all experimentally controlled parameters in a single device: the energy level of the dot, the tunnel couplings to the superconducting leads, the superconducting phase difference across the quantum dot junction, and also an external Zeeman field. The measured phase boundaries are in agreement with the single-impurity Anderson model with superconducting leads as calculated via numerical renormalization group (NRG) [2,55–57] methods and include parameter regimes that have experimentally not been explored before. Finally, we investigate the rates at which the quantum dot switches between doublet and singlet occupation via real-time monitoring of the transmon circuit, allowing us to determine the switching time scales of the quantum dot junction parity across the phase transition.

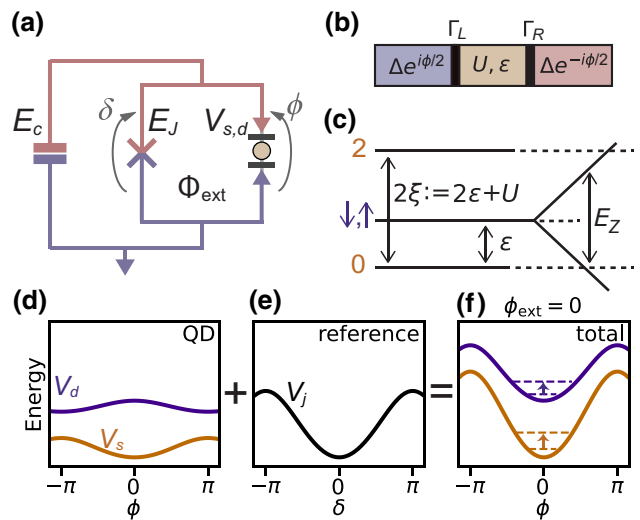


FIG. 1. (a) A schematic diagram of a quantum dot junction incorporated into a transmon circuit. The transmon island with charging energy  $E_c$  is connected to ground by a SQUID formed by the parallel combination of a quantum dot junction and a reference junction. Here,  $\phi$  and  $\delta$  denote the superconducting phase difference across the quantum dot and reference junctions, respectively.  $\Phi_{\text{ext}}$  is the externally applied magnetic flux through the SQUID loop. (b) A model diagram of the quantum dot junction in the excitation picture. Two  $s$ -wave superconductors are connected via tunnel barriers to a single-level quantum dot. (c) A level diagram of the quantum dot hosting zero, one, or two electrons when disconnected from the leads ( $\Gamma_L = \Gamma_R = 0$ ). (d) The phase dependence of the Josephson potential of the quantum dot junction in the singlet (orange) and doublet (purple) state. (e) The Josephson potential of the reference junction. (f) The Josephson potential of the dc SQUID for  $\phi_{\text{ext}} = (2e/\hbar)\Phi_{\text{ext}} = 0$ , with the quantum dot junction in the singlet (orange) and doublet (purple) state. The dashed lines represent the two lowest transmon energy levels in each branch of the Josephson potential, with the arrow denoting the resulting transition frequency, which can differ for the two quantum dot junction states (orange and purple arrows for singlet and doublet, respectively).

## II. DEVICE OVERVIEW

The quantum dot junction under investigation is formed in a  $10\text{-}\mu\text{m}$ -long epitaxial superconductor-semiconductor nanowire with a  $100\text{-nm}$ -wide hexagonal InAs core and a  $6\text{-nm}$ -thick Al shell covering two of its facets [58]. The quantum dot junction is located in a  $200\text{-nm}$ -long uncovered section of the nanowire where the Al has been etched away, where it is electrostatically defined by three bottom gate electrodes [Fig. 2(d)]. As shown in the circuit of Fig. 2(a), this quantum dot junction is placed in parallel to a second Josephson junction, hereafter referred to as the “reference junction,” to form a SQUID. The reference junction consists of a second  $110\text{-nm}$ -long uncovered segment of InAs on the same nanowire as the quantum dot junction. Its Josephson energy  $E_J$  can be tuned with a single gate electrode via the field effect.

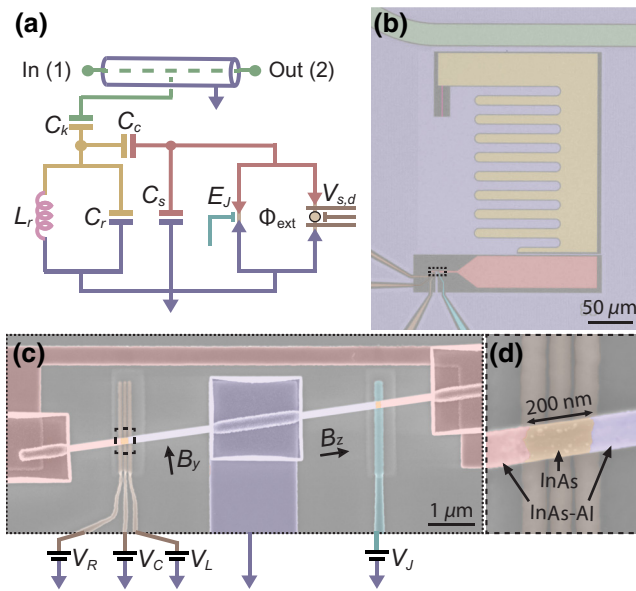


FIG. 2. The device overview. (a) A diagram of the microwave circuit. A coplanar waveguide transmission line (green center conductor) is capacitively coupled to a grounded  $LC$  resonator. The resonator consists of an island (yellow) capacitively and inductively (pink) shunted to ground (blue). The resonator is in turn capacitively coupled to a transmon island (red), which is shunted to ground capacitively as well as via two parallel Josephson junctions. (b) A false-colored optical microscope image of device A, showing the qubit island, the resonator island, the resonator inductor, the transmission line, the electrostatic gates, and ground. (c) A false-colored scanning electron micrograph (SEM) of the Josephson junctions of the transmon, showing the InAs-Al nanowire into which the junctions are defined. The  $B_y$  component of the magnetic field is used to tune  $\Phi_{\text{ext}}$  [60].  $B_z$  is the magnetic field component parallel to the nanowire. (d) A false-colored SEM of the quantum dot junction in which the quantum dot is gate defined. The three bottom gates have a width and spacing of 40 nm, although this is obfuscated by the dielectric layer placed on top [60].

The SQUID connects a superconducting island to ground, resulting in a transmon circuit [59] governed by the Hamiltonian

$$H = -4E_c \partial_\phi^2 + V(\phi), \quad (1)$$

where  $E_c = e^2/2C_\Sigma$ , in which  $C_\Sigma$  is the total capacitance of the island to ground. The Josephson potential  $V(\phi)$  is determined by the phase-dependent energies of the reference junction,  $V_j(\delta) = E_J(1 - \cos \delta)$ , and of the quantum dot junction,  $V_{s,d}(\phi)$ :

$$V(\phi) = E_J [1 - \cos(\phi - \phi_{\text{ext}})] + \begin{cases} V_s(\phi), & \text{singlet}, \\ V_d(\phi), & \text{doublet}. \end{cases} \quad (2)$$

Here, the phase drops across the quantum dot junction ( $\phi$ ) and across the reference junction ( $\delta$ ) are connected according to  $\phi - \delta = \phi_{\text{ext}}$ , where  $\phi_{\text{ext}} = (2e/\hbar)\Phi_{\text{ext}}$  is the phase difference resulting from the externally applied magnetic flux through the SQUID loop,  $\Phi_{\text{ext}}$ .

The presence of the reference junction serves several purposes. First, it allows us to tune the phase difference at the quantum dot junction by changing  $\Phi_{\text{ext}}$  with the  $B_y$  component of the magnetic field [60]. We generally operate the device in a regime where the reference junction has a Josephson energy that is larger than that of the quantum dot by more than an order of magnitude [60]. This ensures that  $\delta$  is close to zero, while  $\phi$  is close to  $\phi_{\text{ext}}$  [61]. Second, the ability to tune  $E_J$  independently of the quantum dot junction ensures that the transition frequencies of the transmon circuit remain inside the measurement bandwidth for all parameter regimes of the quantum dot junction. Finally, the Josephson energy of the reference junction is such that  $E_J/E_c > 25$ , suppressing unwanted sensitivity to fluctuating charges in the environment and justifying the absence of an offset charge in the Hamiltonian of Eq. (1) [59].

In order to perform microwave-spectroscopy measurements, the transmon is capacitively coupled to a readout resonator which is in turn coupled to a transmission line. This allows us to measure the complex microwave transmission  $S_{21}$  of the circuit through the input (1) and output (2) ports of the transmission line.

The experimental implementation of the circuit [Figs. 2(b)-2(d)] differs from conventional circuit-QED geometries in several ways [62], in order to allow the application of magnetic fields in excess of 100 mT. Apart from the Josephson junctions, all circuit elements are made out of field-compatible 20-nm-thick Nb-Ti-N films [63]. We additionally incorporate vortex pinning sites in the ground plane, the transmission line, the resonator island, and the transmon island [64]. We use a lumped-element readout resonator, which has previously been successfully utilized in flux-sensitive devices up to 1 T [65]. Its capacitance is formed by an interdigitated capacitor to ground, while its inductance is formed by a 200-nm-wide Nb-Ti-N nanowire, which has a kinetic inductance of 15 pH/□. This design localizes the regions of high current density at the narrow inductor, where vortices are less likely to nucleate due to its reduced width [66]. For the transmon circuit, the SQUID loop area is chosen to be small, approximately 5  $\mu\text{m}^2$ , in order to suppress flux noise from misalignment in large parallel magnetic fields. Finally, InAs-Al nanowires, in which both junctions are defined, have been shown to support sizeable Josephson energies in fields in excess of 1 T [48,65]. Further details about the device fabrication as well as the cryogenic and room-temperature measurement setup can be found in Sec. II of the Supplemental Material [60].

### III. ANDERSON MODEL FOR A QUANTUM DOT JUNCTION

As we show, the quantum dot junction can be described by a single Anderson impurity tunnel coupled to two superconducting leads. We review its most important properties to facilitate the discussion of the experimental results that follow. In particular, here we discuss the important parameters and concepts that are required to interpret the experimental results, deferring to Sec. I of the Supplemental Material [60] for a technical description of the Hamiltonian and of the numerical methods used to produce the theoretical results.

The model contains a single-level quantum dot coupled to two superconducting leads via tunnel barriers, schematically depicted in Fig. 1(b). The superconducting leads have a pairing gap  $\Delta$  and a phase difference  $\phi$  and the barriers are characterized by single-electron tunneling rates  $\Gamma_L$  and  $\Gamma_R$ . The energy diagram for the isolated quantum dot is shown in Fig. 1(c). The quantum dot is modeled as an Anderson impurity with single-occupancy energy  $\epsilon$ , measured with respect to the Fermi level in the leads, and a repulsive Coulomb interaction  $U$ , which penalizes the double occupancy of the dot energy level.

The quantum dot is spin degenerate at zero magnetic field. An external magnetic field  $B$  splits the degeneracy by a Zeeman energy  $E_Z = g\mu_B B$ , where  $g$  is the effective  $g$  factor of the level and  $\mu_B$  is the Bohr magneton. In the experiment, we choose the  $B$ -field direction to be parallel to the nanowire, since this is the direction that suppresses the superconductivity in the Al nanowire shell the least.

The energy levels of Fig. 1(c) are divided into two sectors, corresponding to their fermion parity or, equivalently, to their total spin  $S$ . The singlet sector includes the states of even parity: the empty state  $|0\rangle$  and the pair state  $|2\rangle$ . These states have  $S = 0$  and are therefore insensitive to the magnetic field  $B$ . The doublet sector includes the states of odd parity,  $|\uparrow\rangle$  and  $|\downarrow\rangle$ , which have  $S = 1/2$ . It is convenient to introduce the energy  $\xi = \epsilon + U/2$ , corresponding to half of the energy gap in the singlet sector, so that  $\xi = 0$  corresponds to the electron-hole symmetry point, where  $|0\rangle$  and  $|2\rangle$  are degenerate in energy. The ground state of the isolated dot (that is,  $\Gamma_L = \Gamma_R = 0$ ) belongs to the doublet sector for  $|\xi| < \frac{1}{2}U$ .

A salient feature of the model is that a quantum phase transition between the doublet and singlet ground state can occur upon changing several experimentally tunable parameters. The dot energy level  $\xi$  and the coupling strengths  $\Gamma_{L,R}$  (all experimentally tunable via the bottom electrostatic gates), as well as the superconducting phase difference  $\phi$  and the magnetic field  $B$ , all act to shift the relative positions of the potentials  $V_s$  and  $V_d$  and to cause an energy crossing between the ground states of the two sectors. In the measurements reported in Secs. IV and V,

we vary all these parameters and compare the extracted phase boundaries to theory.

For the theoretical comparison we use the NRG method [55,67,68] to compute the lowest-lying eigenvalues in the singlet and doublet spin sectors as a function of the phase difference  $\phi$  [69]. This results in the Josephson potentials  $V_s(\phi)$  and  $V_d(\phi)$ , which are then used as input to the model of Eq. (2) to calculate the transmon transition frequencies [60]. The projection onto the lowest-energy state of the Josephson junction in each sector is enough to capture the salient features of our experiment, although the inclusion of excited Andreev states of the quantum dot junction in the circuit model is theoretically possible [35,50,70–72].

Experimentally, the observation of the phase transition is facilitated by the presence of a  $\pi$  phase shift between  $V_s(\phi)$  and  $V_d(\phi)$ . The phase shift arises because the sequence of single-electron tunneling events that leads to the transport of a Cooper pair between the two leads depends on whether the quantum dot is initially in the singlet or the doublet sector. In particular, if the dot is initially in the doublet state, a permutation of spin-up and spin-down electrons is required in order to complete the tunneling sequence [53], leading to a  $\pi$  phase shift due to Fermi-Dirac statistics. Thus, while  $V_s(\phi)$  has a minimum at  $\phi = 0$ , as encountered for conventional Josephson junctions,  $V_d(\phi)$  has a minimum at  $\phi = \pi$  [Fig. 1(d)]. A quantum dot junction in a doublet state is often denominated as a  $\pi$  junction and the singlet-doublet transition is also referred to as the 0- $\pi$  transition. In the following sections, we use the presence or absence of such a  $\pi$  phase shift to identify regions with a singlet or a doublet ground state [73].

### IV. TRANSMON SPECTROSCOPY OF THE QUANTUM DOT

To perform spectroscopy of the resonator, we monitor the microwave transmission  $S_{21}$  across the transmission line while varying the frequency of a single continuous microwave tone,  $f_r$ . This results in a dip with a Lorentzian line shape around the resonance frequency of the lumped-element resonator. Two-tone spectroscopy is subsequently performed by fixing the frequency of this first tone,  $f_r$ , at the minimum of the transmission amplitude,  $|S_{21}|$ , while varying the frequency of a second tone,  $f_t$ , also sent through the transmission line. When the second tone matches the frequency of the transition from ground to the first excited transmon state,  $f_t = f_{01}$ , a peak in  $|S_{21}|$  is observed due to the transmon-state-dependent dispersive shift of the resonator [54]. This gives us access to the transmon transition frequency.

We are interested in the behavior of the device when a single level of the quantum dot provides the dominant contribution to the Josephson effect [69]. To find such a regime, we search for an isolated resonance in the

gate dependence of the frequency spectrum. Isolated resonances often occur when the gate voltages controlling the quantum dot are set close to their pinch-off values [46,47], here operationally defined as the voltage values below which the quantum dot junction does not contribute appreciably to the transition frequency of the transmon. In order to identify the right gate configuration, we perform the following sequence of calibration measurements. First, we characterize the reference junction with the quantum dot pinched off; second, we explore the sizeable parameter space governed by the three quantum dot gates; third, we identify the relation between  $B_y$  and  $\phi_{\text{ext}}$  through the SQUID oscillations of the transmon frequency and find that 2.2 mT corresponds to one flux quantum through the loop; and finally we define appropriate gate coordinates to account for cross-couplings. These calibration measurements are detailed in Sec. III of the Supplemental Material [60]. As a result of this procedure, the gate voltage of the reference junction  $V_J$  is fixed such that the transmon frequency when the quantum dot junction is pinched off is  $f_{01}^0 \approx 4.4$  GHz. Furthermore, we fix  $V_L = 470$  mV and introduce virtual plunger ( $V_P$ ) and right tunnel ( $V_T$ ) gates as a linear combination of  $V_C$  and  $V_R$ , such that, in what follows, the single-particle energy level  $\xi$  is mostly independent of  $V_T$ .

We then move on to study the quantum dot junction. We first monitor the resonator frequency for  $\phi_{\text{ext}} = 0$  while the plunger-gate voltage  $V_P$  is varied [Fig. 3(a)]. This reveals a resonant shape that is discontinuously interrupted near its peak at  $V_P = 395$  mV, followed by other discontinuous jumps in the resonator frequency. An enlargement of the resonance is shown in Fig. 3(b) and the corresponding transmon transition frequency, exhibiting the same discontinuity as the resonator, is shown in Fig. 3(d). We identify regions in  $V_P$  where the transmon frequency  $f_{01}$  is larger and smaller than the reference frequency  $f_{01}^0$ . This hierarchy is reversed upon changing the applied flux to  $\phi_{\text{ext}} = \pi$ , as shown in Figs. 3(c) and 3(e).

These observed discontinuities in frequency are a signature of a singlet-doublet transition. The change of the ground state of the quantum dot junction determines a sudden switch in the branch of the Josephson potential of Eq. (2) (from  $V_s$  to  $V_d$  or vice versa) and, thus, a sudden change in the transmon frequency. This is illustrated numerically in Figs. 3(f) and 3(g), which show the expected evolution of the transmon frequencies as a function of the single-particle energy level  $\xi$ . Here, the transition occurs as  $\xi$  is tuned toward the electron-hole symmetry point  $\xi = 0$ , where the doublet ground state is energetically favorable.

The occurrence of the singlet-doublet transition requires a change of the fermion parity of the quantum dot junction. In the S-QD-S setup, this is possible in the presence of a population of excited quasiparticles in the superconducting leads, providing the required fermion parity reservoir.

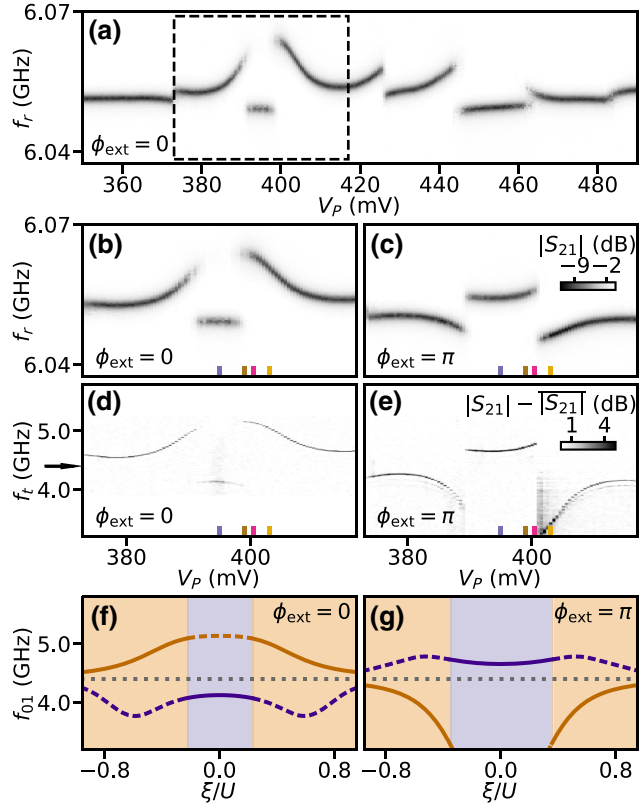


FIG. 3. Spectroscopy of the resonator and the transmon. (a) The  $V_P$  dependence of single-tone spectroscopy for  $\phi_{\text{ext}} = 0$ , showing the transition frequency of the resonator.  $V_P$  is a virtual gate voltage defined as a linear combination of  $V_C$  and  $V_R$  (see text). (b) An enlargement of (a) in the plunger-gate range indicated with dashed lines in (a). (c) The same as (b) but for  $\phi_{\text{ext}} = \pi$ . (d) The  $V_P$  dependence of two-tone spectroscopy for  $\phi_{\text{ext}} = 0$ , showing the transition frequency of the transmon. For each frequency trace,  $|S_{21}| - \bar{|S_{21}|}$  is the magnitude of the transmission minus its average. The black arrow indicates  $f_{01}^0$ , the transmon frequency set by the reference junction when the quantum dot is pinched off. (e) The same as (d) but for  $\phi_{\text{ext}} = \pi$ . For (a)–(e),  $V_T = 182$  mV and  $V_L = 470$  mV. (f) Theoretical estimates of the singlet (orange), doublet (purple), and reference-junction-only (dotted, gray) transmon frequencies as  $\xi$  is varied for  $\phi_{\text{ext}} = 0$ . Solid (dashed) lines indicate which quantum dot occupation corresponds to the ground (excited) state. (g) The same as (f) but for  $\phi_{\text{ext}} = \pi$ . For (f) and (g),  $\Delta/h = 46$  GHz,  $U/\Delta = 12.2$ ,  $\Gamma_L/\Delta = 1.05$ , and  $\Gamma_R/\Delta = 1.12$ .  $f_t$  and  $f_{01}$  denote, respectively, the frequency of the second tone in two-tone spectroscopy and the first transmon transition frequency (see text).

The presence of these quasiparticles should further result in a finite occupation of both the singlet and doublet states when their energy difference is small compared to the effective temperature of the quasiparticle bath, namely in the vicinity of the transition. Indeed, upon closer inspection of the data of Figs. 3(b) and 3(c), both branches of the spectrum are visible in a small frequency window surrounding each discontinuous jump. This is because these

transition spectra are obtained by averaging over many subsequent frequency sweeps, thus reflecting the occupation statistics of the junction. This feature is further discussed in Sec. V.

In Figs. 3(d) and 3(e), the fact that the frequency shift of the transmon has the opposite sign for the singlet and doublet sectors is a consequence of the  $\pi$  phase shift in the Josephson potential between the two sectors. For the case  $\phi_{\text{ext}} = 0$ , the singlet potential interferes constructively with the reference junction potential, while the doublet potential interferes destructively, resulting in  $f_{01} > f_{01}^0$  for the singlet and  $f_{01} < f_{01}^0$  for the doublet. This behavior is reversed when  $\phi_{\text{ext}} = \pi$  and thus serves as a method for identifying the quantum dot-junction state.

## V. SINGLET-DOUBLET TRANSITION BOUNDARIES

Having established a method for identifying singlet and doublet states by transmon spectroscopy, we now experimentally investigate the phase diagrams of the quantum dot junction. We focus on the behavior around  $V_P = 395$  mV and monitor singlet-doublet transitions versus multiple different control parameters.

### A. Plunger gate and flux

We first study the singlet-doublet phase map in  $V_P$  and  $\phi_{\text{ext}}$  space. Figure 4(a) shows the transmon frequency offset with respect to the frequency set by the reference junction,  $\Delta f_{01} = f_{01} - f_{01}^0$ , as a function of  $V_P$  and  $\phi_{\text{ext}}$ . As discussed in Sec. IV, positive values of  $\Delta f_{01}$  result from constructive interference between the two junctions, while negative  $\Delta f_{01}$  values result from destructive interference.

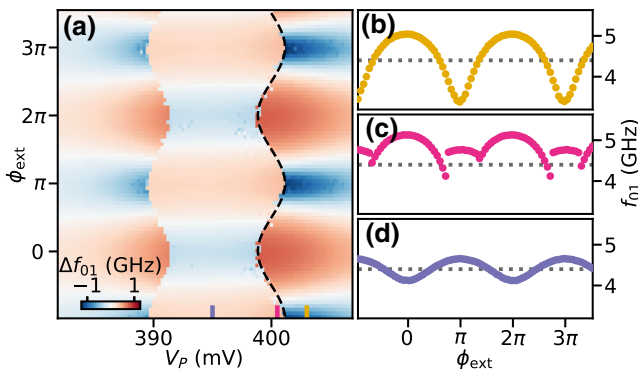


FIG. 4. The flux and plunger-gate dependence. (a) The transmon frequency shift with respect to the frequency set by the reference junction,  $\Delta f_{01} = f_{01} - f_{01}^0$ , versus  $V_P$  and  $\phi_{\text{ext}}$  as extracted from two-tone spectroscopy. The dashed line is a sinusoidal guide for the eye, denoting the transition boundary in line with the theoretical expectation [60]. (b)–(d) Three line cuts of  $f_{01}$  versus  $\phi_{\text{ext}}$  at representative  $V_P$  values, indicated in (a) and Figs. 3(b)–3(e). The dotted line indicates  $f_{01}^0$ . Throughout the figure,  $V_T = 182$  mV.

Going from left to right, three distinct plunger regions can be observed, with a sudden flux offset of exactly  $\pi$  between them [Figs. 4(b) and 4(d)]. We identify the outer two regions as phases with a singlet ground state and the inner region as a doublet ground state. We note that the change in contrast between the two singlet regions suggests that  $V_P$  also weakly tunes  $\Gamma_{L,R}$  in addition to  $\xi$ .

For values of  $V_P$  close to the singlet-doublet transition, we also observe a sinusoidal dependence of the transition boundary on the external flux, resulting in an enhanced region of doublet occupation around  $\phi_{\text{ext}} = \pi$  with respect to  $\phi_{\text{ext}} = 0$ . This comes about from interference between tunneling processes involving the two superconducting leads of the quantum dot junction [4,29], as further discussed in Sec. V B. At a value of  $V_P$  fixed near this boundary, we thus also observe a singlet-doublet transition versus the external flux [Fig. 4(c)].

In Fig. 4 and subsequent figures, the transition boundary between the singlet and doublet phase appears to be sharp and not affected by the thermal broadening typical of transport experiments [20–22,28–30]. The sharpness is a result of a selective spectroscopy technique. As detailed in Sec. III.E of the Supplemental Material [60], in the vicinity of a transition, two resonant dips appear in single-tone spectroscopy, one for the singlet and one for the doublet. In this circumstance, the center frequency of either dip can be chosen as the readout frequency for the subsequent two-tone spectroscopy measurement. This binary choice selects the transmon transition frequency belonging to the corresponding quantum dot-junction state. It is reasonable to assume that the most prominent dip corresponds to the state of the quantum dot junction, which is more prominently occupied and thus lower in energy. If this is the case, the extracted phase boundaries are a close approximation to the zero-temperature phase diagram of the quantum dot junction. We note that when the occupations of the singlet and doublet states are almost equally probable, the selective spectroscopy method is affected by selection errors, which leads to the pixelation effects visible in Fig. 4 near the phase boundaries. In Sec. VI, we explicitly measure the lifetimes of the quantum dot in the singlet and doublet states, substantiating the latter statements.

### B. Tunnel gate

Next, we explore the singlet-doublet transition in plunger and tunnel gate space, where the tunnel gate is expected to control the tunnel rates between the quantum dot and the leads,  $\Gamma_{L,R}$ . Figure 5(a) shows  $\Delta f_{01}$  versus the plunger and tunnel gates at  $\phi_{\text{ext}} = 0$ . The region of doublet occupancy ( $\Delta f_{01} < 0$ ) takes the shape of a dome, similar to the one coarsely seen in flux-insensitive tunneling spectroscopy experiments [14,17]. This shape is in accordance with theoretical expectations for the boundary in the  $\xi$ - $\Gamma$  plane. Its physical origin depends on the parameter

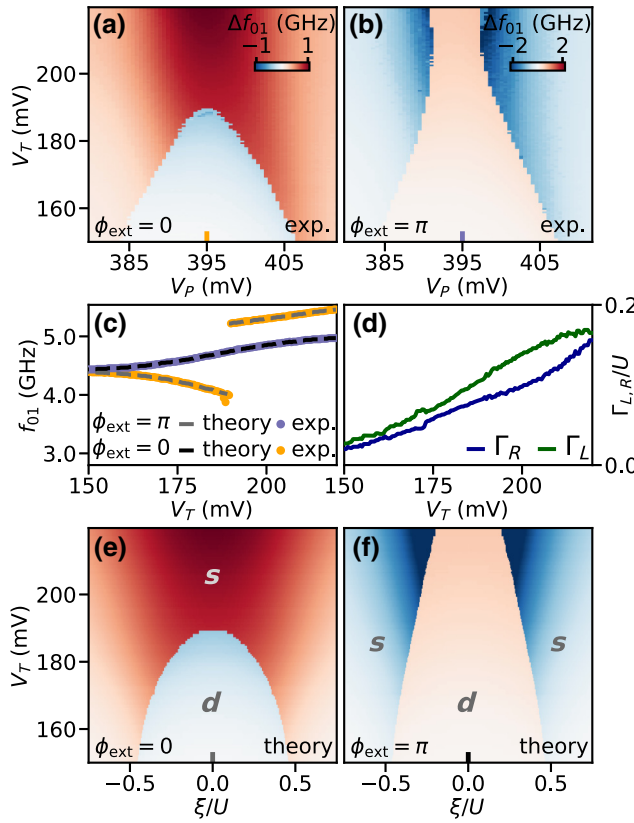


FIG. 5. The tunnel gate dependence. (a)  $\Delta f_{01}$  versus  $V_P$  and  $V_T$  at  $\phi_{\text{ext}} = 0$ , where  $V_T$  is a virtual gate voltage defined as a linear combination of  $V_C$  and  $V_R$  (see text). The blue region corresponds to a negative supercurrent contribution from the quantum dot junction, while the red region corresponds to a positive contribution. (b) The same measurement as (a) repeated for  $\phi_{\text{ext}} = \pi$ . (c) Line cuts of (a) and (b) at  $V_P = 395$  mV overlaid with best fits based on NRG calculations. (d) The extracted dependence of  $\Gamma_{L,R}$  on  $V_T$ . (e) The calculated transmon frequencies based on NRG calculations at  $\phi_{\text{ext}} = 0$  as matched to the measured data, with the  $V_T$  axis as given in (d). The color bar is shared with (a). (f) The same as (e) but for  $\phi_{\text{ext}} = \pi$ , with the same color bar as (b). For the NRG calculations in (c)–(f) we fix  $\Delta/h = 46$  GHz and  $U/\Delta = 12.2$ .

regime [9]. For  $U \ll \Delta$ , it arises due to an increase in induced superconductivity on the dot with increasing values of  $\Gamma$ , favoring BCS-like singlet occupation. For  $U \gg \Delta$ , it instead comes about from increased antiferromagnetic Kondo exchange interactions between the spin on the dot and the quasiparticles in the leads, favoring a Yu-Shiba-Rusinov- (YSR) like singlet occupation. In both regimes, the singlets compete with doublets, ultimately determining the transition to a singlet ground state at large enough  $\Gamma = \Gamma_L + \Gamma_R$ .

We investigate the same plunger and tunnel gate dependence at an external flux  $\phi_{\text{ext}} = \pi$  [see Fig. 5(b)]. We find that the doublet phase is enhanced considerably compared to  $\phi_{\text{ext}} = 0$ , due to the previously mentioned interference

between tunneling processes to the superconducting leads. Notably, rather than a domelike shape, the phase boundary takes a characteristic “chimney” shape that has been theoretically predicted [4] but, to our knowledge, not yet confirmed experimentally before these measurements. Unlike the dome, the chimney does not close for any  $V_T$ . In an extended gate range, it is seen to connect to another doublet region of the parameter space, which is disconnected from the dome of Fig. 5(a) at  $\phi_{\text{ext}} = 0$  (see Sec. III.D of the Supplemental Material [60]).

The chimney at  $\phi_{\text{ext}} = \pi$  is much less thoroughly researched than the dome at  $\phi_{\text{ext}} = 0$ . The open questions include that of the exact nature of the doublet states as a function of the  $U/\Delta$  and  $\Gamma/U$  ratios, and the role of the flux bias [74–77]. In particular, when  $U \gg \Delta$ , the doublet state for small  $\Gamma$  is a decoupled doublet state with a single local moment in the quantum dot. On the other hand, in the same limit but at large  $\Gamma$  (i.e., in the neck of the chimney), the strong exchange interaction with both superconductors is expected to lead to some mixing with the doublet states that involve one Bogoliubov quasiparticle from each lead [78], causing an overscreening of the local moment in the quantum dot. The role of the exchange interaction is also more pronounced at  $\phi_{\text{ext}} = \pi$  because the anomalous component of the hybridization (describing the proximity effect) is suppressed due to the cancellation of contributions from the left and right leads [76], whereas the cancellation is exact when  $\Gamma_L = \Gamma_R$ . This further stabilizes the spin-doublet states. The experimental observation of the chimney calls for more thorough theoretical studies of this parameter regime of the model.

We compare the results at both values of the external flux to the expected transition frequencies obtained from NRG calculations. We assume that  $\xi = 0$  occurs at  $V_P = 395$  mV, since this is the symmetry point of the experimental data. At this point, by requiring simultaneous agreement between experiment and theory for both values of external flux [Fig. 5(c)], we are able to extract several of the model parameters. We find that  $\Delta/h = 46$  GHz (190  $\mu$ eV), close to the bulk value of Al. We furthermore extract  $U/\Delta = 12.2$ , corresponding to a sizeable charging energy of 2.3 meV. This places the nature of the singlets near  $\xi = 0$  in the strongly correlated regime, with a YSR-like character rather than a BCS-like one. By matching values of  $\Gamma_{L,R}$  to  $V_T$ , we then find that  $\Gamma/U$  varies between 0.05 and 0.4, while  $\Gamma_R/\Gamma_L \approx 0.75 - 1$  in the range of gates explored [Fig. 5(d)]. The details of the numerical procedure as well as error estimation can be found in Sec. I.C of the Supplemental Material [60], including estimates based on an alternative potential shape for the reference junction.

The extracted set of parameters is consistent with the observed dome shape at  $\phi_{\text{ext}} = 0$ , as shown in Fig. 5(e). Additionally, as a result of the ratio  $\Gamma_R/\Gamma_L$  remaining close to 1, the extracted parameters also match the observed

diverging behavior at  $\phi_{\text{ext}} = \pi$  [Fig. 5(f)], which is not enforced in the parameter extraction. In these figures, we do not map  $V_P$  to  $\xi$  beyond identifying  $V_P = 395$  mV with  $\xi = 0$ , as a unique mapping cannot be constructed due to the unintended dependence of  $\Gamma$  on  $V_P$ . We speculate that this causes the remaining discrepancies between the measured and calculated boundaries in the horizontal direction.

### C. Magnetic field parallel to the nanowire

Finally, we investigate the effect of a magnetic field applied parallel to the nanowire on the phase-transition boundaries. Here, we expect a magnetic-field-induced singlet-doublet transition to occur [14,18,19]. As  $B_z$  increases, the doublet sector separates into spin species that are aligned and antialigned with respect to the magnetic field, dispersing in opposite energy directions. The singlet ground-state energy, on the other hand, is approximately independent of the magnetic field. Given an appropriate zero-field energy-level configuration, for some  $B_z$  value, the energy of one of the two doublet states will thus become lower than that of the singlet and become the ground state instead [see Fig. 1(c)].

Such a transition will only occur for specific configurations of  $V_P$  and  $V_T$  in the experimentally accessible range of magnetic fields. We therefore start by applying  $B_z = 200$  mT parallel to the nanowire axis, a sizeable magnetic field, yet one for which the  $E_J$  of the reference junction is not yet substantially suppressed [60]. At this field, we investigate the effect on the  $V_P$  and  $V_T$  phase map. The result, shown in Figs. 6(a) and 6(b), reveals an expansion of the doublet region for both  $\phi_{\text{ext}} = 0$  and  $\phi_{\text{ext}} = \pi$ . We can classify different regions in the parameter space by comparing the phase boundaries at  $B_z = 10$  mT and  $B_z = 200$  mT. There are regions in which a singlet ground state remains a singlet ground state, independent of the flux and the magnetic field, as well as regions where a singlet-doublet transition occurs depending on the value of the

flux. However, there is also a region that starts off as a singlet ground state and ends up as a doublet ground state at high field, for all values of the flux. Thus, fixing  $V_P$  and  $V_T$  in this region, we expect to observe a transition with  $B_z$  for any value of  $\phi_{\text{ext}}$ . A measurement of  $\Delta f_{01}$  versus  $\phi_{\text{ext}}$  and  $B_z$  [Fig. 6(c)] indeed reveals such a transition, occurring at a different magnetic field depending on the external flux value. For details about the data analysis and identification of the flux axis, we refer to Sec. IV of the Supplemental Material [60].

## VI. DYNAMICS OF THE SINGLET-DOUBLET TRANSITION

In the preceding sections, we make use of selective spectroscopy to reconstruct the phase-transition boundaries. We now turn to time-resolved spectroscopy techniques to study the parity dynamics of the quantum dot junction close to the transition, aiming to characterize the lifetimes of singlet (even-parity) and doublet (odd-parity) states. These methods have previously been used to study quasi-particle dynamics in superconducting qubits [48,79] and have recently also been applied to a nanowire junction to study the poisoning of Andreev bound states [33,45,80].

To resolve individual switching events, we use a second device (device B) with a larger signal-to-noise ratio (SNR) than the device used for the preceding sections (device A), enabling the use of short acquisition times. Device B is nearly identical to device A, except for two features meant to increase the SNR: (1) a stronger coupling between the resonator and the transmission line; and (2) an additional capacitor at its input port, which increases the directionality of the outgoing signal [81]. On device B, we perform measurements on microsecond time scales by directly monitoring changes in the outgoing signal at a fixed readout frequency. A continuous measurement of the outgoing microwave field then reveals a random telegraph signal between two different levels, a consequence of the switches in the quantum dot junction parity [Figs. 7(a)

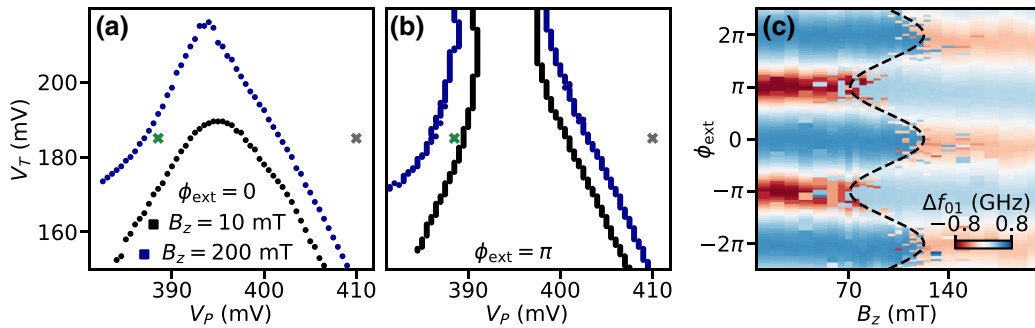


FIG. 6. The parallel magnetic field dependence. (a) The borders between the singlet and doublet regions for  $B_z = 10$  mT (black) and  $B_z = 200$  mT (blue), measured at  $\phi_{\text{ext}} = 0$ . (b) The same as (a) but for  $\phi_{\text{ext}} = \pi$ . The gray marker denotes the gate point used to recalibrate the flux axis after varying  $B_z$  [60]. (c)  $\Delta f_{01}$  versus  $B_z$  and  $\phi_{\text{ext}}$ , measured at the gate point indicated in (a) and (b) with a green marker. The sinusoidal dashed line serves as a guide for the eye, in line with the transition boundary expected from theory [60].

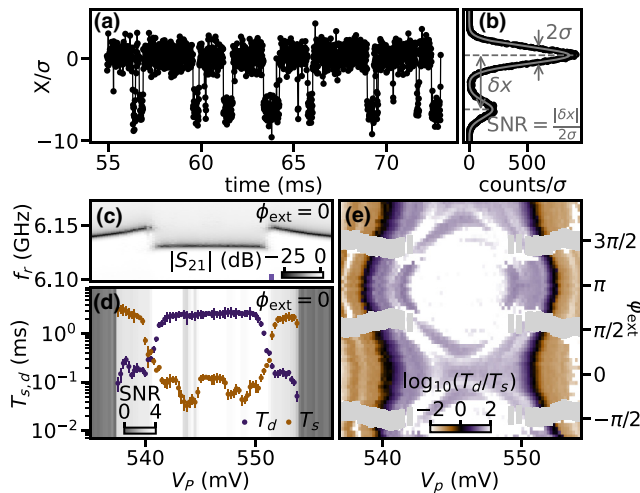


FIG. 7. The dependence of the parity lifetimes on  $V_P$  and  $\phi_{ext}$  for device B. (a) A 18-ms cut of a continuously measured time trace integrated in time bins of  $t_{int} = 11.4\mu s$ , revealing jumps between two distinct states.  $X$  is the common axis onto which the quadratures of the outgoing microwave field are rotated to obtain the highest SNR, which takes a value of 3.3 here. (b) A one-dimensional histogram of the response in (a) (black) and the best fit of a double Gaussian line shape (gray). The separation of their centers  $\delta x$  and their width  $\sigma$  together define the SNR. The ratio of their amplitudes determines the ratio of the lifetimes. For (a) and (b),  $V_P = 551.4$  mV and  $\phi_{ext} = 0$ . (c) The  $V_P$  dependence of  $|S_{21}|$  at  $\phi_{ext} = 0$ . (d) The  $V_P$  dependence of the extracted lifetimes at  $\phi_{ext} = 0$ . The markers indicate the mean, while the error bars indicate the maximum and minimum values of ten consecutive 2-s time traces. The SNR is shown in gray scale in the background. For points where  $\text{SNR} < 1$ , the extracted lifetimes are discarded. (e) A two-dimensional map of  $\log_{10}(T_d/T_s)$  versus  $V_P$  and  $\phi_{ext}$ , extracted from a 2-s time trace for each pixel. White pixels indicate points at which  $\text{SNR} < 1$ , while gray regions indicate where the resonator frequencies of singlet and doublet states overlap and thus cannot be distinguished.

and 7(b)]. Owing to the increased temporal resolution of the detection method, even short-lived excited state occupation can now be detected. The characteristic time scales of the telegraph signal reflect the underlying lifetimes of the singlet and doublet states,  $T_s$  and  $T_d$ , or, equivalently, their decay rates,  $\Gamma_s = 1/T_s$  and  $\Gamma_d = 1/T_d$ . These quantities can be extracted via a spectral analysis of the time traces, as described in Sec. V of the Supplemental Material [60].

To investigate the switching dynamics, we tune device B to a regime similar to that of Sec. VA, studied in device A. By measuring  $S_{21}$  with single-tone spectroscopy, we once more find ground-state transitions between singlet and doublet as a function of  $V_P$  [Fig. 7(c)]. The discontinuous resonant shape, akin to that of Fig. 3(b), is symmetric around  $V_P = 546$  mV, which we identify with  $\xi = 0$ . The singlet and doublet resonant frequencies are simultaneously visible close to the discontinuity at the transition.

The time-resolved measurements over the same gate voltage range reveal a smooth but strong evolution of the parity lifetimes with  $V_P$  [Fig. 7(d)]. The hierarchy of lifetimes inverts as  $V_P$  is tuned across the phase transition, reflecting the change in the ground-state parity. Away from the transition, in either the singlet or doublet phase, we observe the lifetime in the ground-state sector to be on the order of several milliseconds, exceeding that of the excited state by more than an order of magnitude. These numbers are very favorable for the implementation of Andreev pair qubits [32] as well as Andreev spin qubits [33,34,45], the control of which has so far been limited by microsecond parity lifetimes.

We further explore the evolution of the relative lifetimes versus  $V_P$  and  $\phi_{ext}$ . Figure 7(e) shows a two-dimensional map of  $\log_{10}(T_d/T_s)$ , which is a measure of the lifetime asymmetry. We find behavior similar to that previously seen in Fig. 4, with a sinusoidal boundary of equal rates, indicative of the singlet-doublet transition. Furthermore, we observe a strong polarization of the junction parity inside the doublet phase ( $T_d \gg T_s$ ), where the SNR eventually becomes limited by our ability to resolve the rare and short-lived switches out of the ground state. Additionally, we find a modulation of  $T_d$  with flux, with longer lifetimes at  $\phi_{ext} = \pi$  [60]. This flux dependence likely originates from the oscillation of the singlet-doublet energy gap with flux but might also be indicative of a coherent suppression of the tunneling rates. The polarization of the junction parity also occurs inside the singlet phase, where  $T_s \gg T_d$  for  $V_P$  values away from the transition [Fig. 7(d)].

Strong parity polarization may not be surprising for a system in thermal equilibrium at temperatures below 100 mK, typical of these experiments, corresponding to a thermal energy that is small compared to the singlet-doublet energy difference away from the transition. However, parity lifetimes in superconducting circuits are seldom determined by thermal fluctuations but, rather, by highly energetic nonequilibrium quasiparticles [82]. While such nonequilibrium quasiparticles are most likely also present in our device, we believe that their influence is suppressed by the large charging energy of the quantum dot junction.

Finally, we observe a nonmonotonic variation of the rate asymmetry inside both the singlet and doublet phase, forming apparent contours of fixed lifetimes [Fig. 7(e)]. We hypothesize two possible reasons behind this structure in the data: it could be caused by parity pumping mechanisms where the readout tone is resonant with the energy difference between singlet and doublet [80], as well as by the spectral density of the nonequilibrium quasiparticles present in the environment [83]. Further investigation of the tunnel gate, power, and temperature dependence of the rate asymmetry can be found in Sec. VI of the Supplemental Material [60]; we leave a more detailed study for future work.

## VII. CONCLUSIONS

We demonstrate the use of a transmon circuit to sensitively detect the ground-state parity of a quantum dot Josephson junction. The transition frequency of the transmon exhibits a discontinuity if the ground state of the device changes from a singlet to a doublet, due to the presence of a  $\pi$  phase shift in the Josephson potential of the junction. This allows us to accurately reconstruct the occurrence of the singlet-doublet transition as a function of all control parameters available in a single device, matching them to those expected from NRG calculations of an Anderson impurity model. In particular, we observe the flux-induced enhancement of the doublet phase, in the form of the striking transformation of a dome-shaped phase boundary at  $\phi_{\text{ext}} = 0$  into a chimney-shaped phase boundary at  $\phi_{\text{ext}} = \pi$  (Fig. 5).

In future research, this singlet-doublet tuning capability could become beneficial for several applications. First, it can be used to define and control Andreev-pair and spin qubits and to couple them to conventional superconducting qubits. Second, tuning the dot to the doublet phase is a robust way to induce a  $\pi$  phase shift, which could be exploited to define a hybrid 0- $\pi$  qubit that does not rely on the fine tuning of the applied flux [84]. Third, it can facilitate the bottom-up realization of a topological superconductor from a chain of proximitized quantum dots [85–87]. Finally, fast gate or flux-based switching between the 0 and  $\pi$  shift of the dot can also be of interest for applications in Josephson magnetic random access memory (JMRAM) technologies [88].

We subsequently use continuous-time-domain monitoring of the transmon resonant frequency to determine the lifetimes of singlet and doublet states. We find that the time between switching events is strongly enhanced when the quantum dot is tuned away from the phase transition. Since our estimates indicate that  $U \gg \Delta$  in our devices, we attribute this effect to the large energy difference associated with charging the quantum dot. These findings are encouraging for Andreev qubits, which benefit from long parity lifetimes, and suggest that large- $U$  quantum dots could be effective as filters for high-energy quasiparticles. However, further work is required to understand the full dependence of parity lifetimes on  $U$ .

In this work, we focus on the study of a single-level quantum dot by tuning our junction very close to pinch-off. Looking forward, there is much left to explore in the parameter space of such a device. To begin with, it would be interesting to understand whether the crossover from the BCS-like to the YSR-like singlet has any signature in the microwave response of the system. Second, opening the junction further brings the quantum dot into a multilevel regime, not captured by the single-impurity Anderson model and still largely unexplored. Finally, while we primarily study the ground-state properties of

the quantum dot junction, microwave spectroscopy should allow us to study its excitations—as, e.g., recently demonstrated in Refs. [49,52], particularly at  $\phi_{\text{ext}} = \pi$ .

Further work will also aim at elucidating the role of spin-orbit coupling in the quantum dot junction. It is well known that, when time-reversal invariance is broken, spin-orbit coupling can induce a spin-splitting of energy levels in the doublet sector [36,37,44], which is essential for Andreev spin qubits. While this effect could have been expected to occur in the measurements presented here, it is not detected; we speculate that the level spacing in the dot is too large to result in a significant splitting [37].

Important extensions of our work could arise if the hybrid nanowire in our microwave circuit is driven into the Majorana topological phase [70–72,89], which is currently challenging because of a large parameter space [90] and because of demanding disorder requirements [91]. The inclusion of a quantum dot in a Josephson junction between two topological superconductors could be beneficial for the detection of the  $4\pi$  Josephson effect: as we see, it mitigates quasiparticle poisoning, although it would not resolve [92] the problem of distinguishing Majorana zero modes from trivial zero-energy Andreev bound states [93]. Finally, the manipulation of quantum dots coupled to superconducting leads is an essential ingredient of scalable proposals for topological quantum computation [40].

The data and analysis code that support the findings of this study are openly available in 4TU.ResearchData at Ref. [108].

## ACKNOWLEDGMENTS

We acknowledge fruitful discussions with Gijs de Lange, and we thank Valla Fatemi, Pavel Kurilovich, Max Hays, Spencer Diamond, Nick Frattini, and Vladislav Kurilovich for sharing their related work [52] prior to its publication and for productive discussions. We also thank Valla Fatemi and Pavel Kurilovich for their feedback on this manuscript. We further thank Peter Krogstrup for guidance in the material growth, Daniël Bouman for nanowire placement, and James Kroll for help with nanofabrication. This research is co-funded by the allowance for Top Consortia for Knowledge and Innovation (TKIs) from the Dutch Ministry of Economic Affairs, research project “Scalable circuits of Majorana qubits with topological protection” (i39, SCMQ) with project number 14SCMQ02, from the Dutch Research Council (NWO), and the Microsoft Quantum initiative. R.Ž. acknowledges the support of the Slovenian Research Agency (ARRS) under P1-0044, P1-0416, and J1-3008. R.A. acknowledges support from the Spanish Ministry of Science and Innovation through Grant No. PGC2018-097018-B-I00 (AEI/FEDER, EU) and from the CSIC Research Platform on Quantum Technologies PTI-001. B.v.H. was partially supported by the Dutch Research Council (NWO).

A.B., M.P.V., B.v.H., and A.K. conceived the experiment. Y.L. developed and provided the nanowire materials. A.B., M.P.V., L.S., L.G., and J.J.W prepared the experimental setup and the data-acquisition tools. L.S. deposited the nanowires. A.B. and M.P.V. designed and fabricated the device, performed the measurements, and analyzed the data, with continuous feedback from L.S., L.G., J.J.W., C.K.A., A.K., and B.v.H. R.A., J.A., B.v.H., and R.Z. provided theory support during and after the measurements and formulated the theoretical framework to analyze the experiment. R.Z. performed the NRG calculations. A.B., M.P.V., and B.v.H. wrote the code to compute the circuit energy levels and extract experimental parameters. L.P.K., R.A., A.K., and B.v.H. supervised the work. A.B., M.P.V., R.Z., and B.v.H. wrote the manuscript, with feedback from all authors.

- [1] L. I. Glazman and K. A. Matveev, Resonant Josephson current through Kondo impurities in a tunnel barrier, *JETP Lett.* **49**, 570 (1989).
- [2] T. Yoshioka and Y. Ohashi, Numerical renormalization group studies on single impurity Anderson model in superconductivity: A unified treatment of magnetic, nonmagnetic impurities, and resonance scattering, *J. Phys. Soc. Jpn.* **69**, 1812 (2000).
- [3] M.-S. Choi, M. Lee, K. Kang, and W. Belzig, Kondo effect and Josephson current through a quantum dot between two superconductors, *Phys. Rev. B* **70**, 020502(R) (2004).
- [4] A. Oguri, Y. Tanaka, and A. C. Hewson, Quantum phase transition in a minimal model for the Kondo effect in a Josephson junction, *J. Phys. Soc. Jpn.* **73**, 2494 (2004).
- [5] Y. Tanaka, A. Oguri, and A. C. Hewson, Kondo effect in asymmetric Josephson couplings through a quantum dot, *New J. Phys.* **9**, 115 (2007).
- [6] A. Martín-Rodero and A. Levy Yeyati, Josephson and Andreev transport through quantum dots, *Adv. Phys.* **60**, 899 (2011).
- [7] C. Karrasch, A. Oguri, and V. Meden, Josephson current through a single Anderson impurity coupled to BCS leads, *Phys. Rev. B* **77**, 024517 (2008).
- [8] D. J. Luitz, F. F. Assaad, T. Novotný, C. Karrasch, and V. Meden, Understanding the Josephson Current through a Kondo-Correlated Quantum Dot, *Phys. Rev. Lett.* **108**, 227001 (2012).
- [9] A. Kadlecová, M. Žonda, V. Pokorný, and T. Novotný, Practical Guide to Quantum Phase Transitions in Quantum-Dot-Based Tunable Josephson Junctions, *Phys. Rev. Appl.* **11**, 044094 (2019).
- [10] V. Meden, The Anderson-Josephson quantum dot—a theory perspective, *J. Phys. Condens. Matter* **31**, 163001 (2019).
- [11] J. D. Pillet, C. H. L. Quay, P. Morfin, C. Bena, A. Levy Yeyati, and P. Joyez, Andreev bound states in supercurrent-carrying carbon nanotubes revealed, *Nat. Phys.* **6**, 965 (2010).
- [12] J.-D. Pillet, P. Joyez, R. Žitko, and M. F. Goffman, Tunneling spectroscopy of a single quantum dot coupled to a superconductor: From Kondo ridge to Andreev bound states, *Phys. Rev. B* **88**, 045101 (2013).
- [13] R. S. Deacon, Y. Tanaka, A. Oiwa, R. Sakano, K. Yoshida, K. Shibata, K. Hirakawa, and S. Tarucha, Tunneling Spectroscopy of Andreev Energy Levels in a Quantum Dot Coupled to a Superconductor, *Phys. Rev. Lett.* **104**, 076805 (2010).
- [14] E. J. H. Lee, X. Jiang, M. Houzet, R. Aguado, C. M. Lieber, and S. D. Franceschi, Spin-resolved Andreev levels and parity crossings in hybrid superconductor-semiconductor nanostructures, *Nat. Nanotechnol.* **9**, 79 (2014).
- [15] W. Chang, V. E. Manucharyan, T. S. Jespersen, J. Nygård, and C. M. Marcus, Tunneling Spectroscopy of Quasiparticle Bound States in a Spinful Josephson Junction, *Phys. Rev. Lett.* **110**, 217005 (2013).
- [16] S. Li, N. Kang, P. Caroff, and H. Q. Xu, 0- $\pi$  phase transition in hybrid superconductor-InSb nanowire quantum dot devices, *Phys. Rev. B* **95**, 014515 (2017).
- [17] E. J. H. Lee, X. Jiang, R. Žitko, R. Aguado, C. M. Lieber, and S. De Franceschi, Scaling of subgap excitations in a superconductor-semiconductor nanowire quantum dot, *Phys. Rev. B* **95**, 180502(R) (2017).
- [18] M. Valentini, F. Peñaranda, A. Hofmann, M. Brauns, R. Hauschild, P. Krogstrup, P. San-Jose, E. Prada, R. Aguado, and G. Katsaros, Nontopological zero-bias peaks in full-shell nanowires induced by flux-tunable Andreev states, *Science* **373**, 82 (2021).
- [19] A. M. Whiticar, A. Fornieri, A. Banerjee, A. C. C. Drachmann, S. Gronin, G. C. Gardner, T. Lindemann, M. J. Manfra, and C. M. Marcus, Zeeman-driven parity transitions in an Andreev quantum dot, arXiv e-prints (2021), [ArXiv:2101.09706](https://arxiv.org/abs/2101.09706).
- [20] J. A. van Dam, Y. V. Nazarov, E. P. A. M. Bakkers, S. D. Franceschi, and L. P. Kouwenhoven, Supercurrent reversal in quantum dots, *Nature* **442**, 667 (2006).
- [21] J. P. Cleuziou, W. Wernsdorfer, V. Bouchiat, T. Ondarcuhu, and M. Monthioux, Carbon nanotube superconducting quantum interference device, *Nat. Nanotechnol.* **1**, 53 (2006).
- [22] H. I. Jørgensen, T. Novotný, K. Grove-Rasmussen, K. Flensberg, and P. E. Lindelof, Critical current 0- $\pi$  transition in designed Josephson quantum dot junctions, *Nano Lett.* **7**, 2441 (2007).
- [23] H. I. Jørgensen, K. Grove-Rasmussen, K. Flensberg, and P. E. Lindelof, Critical and excess current through an open quantum dot: Temperature and magnetic-field dependence, *Phys. Rev. B* **79**, 155441 (2009).
- [24] A. Eichler, R. Deblock, M. Weiss, C. Karrasch, V. Meden, C. Schönenberger, and H. Bouchiat, Tuning the Josephson current in carbon nanotubes with the Kondo effect, *Phys. Rev. B* **79**, 161407(R) (2009).
- [25] E. J. H. Lee, X. Jiang, R. Aguado, G. Katsaros, C. M. Lieber, and S. De Franceschi, Zero-Bias Anomaly in a Nanowire Quantum Dot Coupled to Superconductors, *Phys. Rev. Lett.* **109**, 186802 (2012).
- [26] R. Maurand, T. Meng, E. Bonet, S. Florens, L. Marty, and W. Wernsdorfer, First-Order 0- $\pi$  Quantum Phase Transition in the Kondo Regime of a Superconducting Carbon-Nanotube Quantum Dot, *Phys. Rev. X* **2**, 011009 (2012).

- [27] A. Kumar, M. Gaim, D. Steininger, A. Levy Yeyati, A. Martín-Rodero, A. K. Hüttel, and C. Strunk, Temperature dependence of Andreev spectra in a superconducting carbon nanotube quantum dot, *Phys. Rev. B* **89**, 075428 (2014).
- [28] D. B. Szombati, S. Nadj-Perge, D. Car, S. R. Plissard, E. P. A. M. Bakkers, and L. P. Kouwenhoven, Josephson  $\phi_0$ -junction in nanowire quantum dots, *Nat. Phys.* **12**, 568 (2016).
- [29] R. Delagrange, D. J. Luitz, R. Weil, A. Kasumov, V. Meden, H. Bouchiat, and R. Deblock, Manipulating the magnetic state of a carbon nanotube Josephson junction using the superconducting phase, *Phys. Rev. B* **91**, 241401(R) (2015).
- [30] R. Delagrange, R. Weil, A. Kasumov, M. Ferrier, H. Bouchiat, and R. Deblock, 0- $\pi$  quantum transition in a carbon nanotube Josephson junction: Universal phase dependence and orbital degeneracy, *Phys. B: Condens. Matter* **536**, 211 (2018).
- [31] A. García Corral, D. M. T. van Zanten, K. J. Franke, H. Courtois, S. Florens, and C. B. Winkelmann, Magnetic-field-induced transition in a quantum dot coupled to a superconductor, *Phys. Rev. Res.* **2**, 012065(R) (2020).
- [32] C. Janvier, L. Tosi, L. Bretheau, Ç. Girit, M. Stern, P. Bertet, P. Joyez, D. Vion, D. Esteve, M. F. Goffman, H. Pothier, and C. Urbina, Coherent manipulation of Andreev states in superconducting atomic contacts, *Science* **349**, 1199 (2015).
- [33] M. Hays, V. Fatemi, K. Serniak, D. Bouman, S. Diamond, G. de Lange, P. Krogstrup, J. Nygård, A. Geresdi, and M. H. Devoret, Continuous monitoring of a trapped superconducting spin, *Nat. Phys.* **16**, 1103 (2020).
- [34] M. Hays, V. Fatemi, D. Bouman, J. Cerrillo, S. Diamond, K. Serniak, T. Connolly, P. Krogstrup, J. Nygård, A. Levy Yeyati, A. Geresdi, and M. H. Devoret, Coherent manipulation of an Andreev spin qubit, *Science* **373**, 430 (2021).
- [35] A. Zazunov, V. S. Shumeiko, E. N. Bratus', J. Lantz, and G. Wendin, Andreev Level Qubit, *Phys. Rev. Lett.* **90**, 087003 (2003).
- [36] N. M. Chtchelkatchev and Y. V. Nazarov, Andreev Quantum Dots for Spin Manipulation, *Phys. Rev. Lett.* **90**, 226806 (2003).
- [37] C. Padurariu and Y. V. Nazarov, Theoretical proposal for superconducting spin qubits, *Phys. Rev. B* **81**, 144519 (2010).
- [38] L. Pavešić and R. Žitko, Qubit based on spin-singlet Yu-Shiba-Rusinov states, *Phys. Rev. B* **105**, 075129 (2022).
- [39] S. Plugge, A. Rasmussen, R. Egger, and K. Flensberg, Majorana box qubits, *New J. Phys.* **19**, 012001 (2017).
- [40] T. Karzig, C. Knapp, R. M. Lutchyn, P. Bonderson, M. B. Hastings, C. Nayak, J. Alicea, K. Flensberg, S. Plugge, Y. Oreg, C. M. Marcus, and M. H. Freedman, Scalable designs for quasiparticle-poisoning-protected topological quantum computation with Majorana zero modes, *Phys. Rev. B* **95**, 235305 (2017).
- [41] T. B. Smith, M. C. Cassidy, D. J. Reilly, S. D. Bartlett, and A. L. Grimsmo, Dispersive Readout of Majorana Qubits, *PRX Quantum* **1**, 020313 (2020).
- [42] G. de Lange, B. van Heck, A. Bruno, D. J. van Woerkom, A. Geresdi, S. R. Plissard, E. P. A. M. Bakkers, A. R. Akhmerov, and L. DiCarlo, Realization of Microwave Quantum Circuits Using Hybrid Superconducting-Semiconducting Nanowire Josephson Elements, *Phys. Rev. Lett.* **115**, 127002 (2015).
- [43] T. W. Larsen, K. D. Petersson, F. Kuemmeth, T. S. Jespersen, P. Krogstrup, J. Nygård, and C. M. Marcus, Semiconductor-Nanowire-Based Superconducting Qubit, *Phys. Rev. Lett.* **115**, 127001 (2015).
- [44] L. Tosi, C. Metzger, M. Goffman, C. Urbina, H. Pothier, S. Park, A. Levy Yeyati, J. Nygård, and P. Krogstrup, Spin-Orbit Splitting of Andreev States Revealed by Microwave Spectroscopy, *Phys. Rev. X* **9**, 011010 (2019).
- [45] M. Hays, G. de Lange, K. Serniak, D. J. van Woerkom, D. Bouman, P. Krogstrup, J. Nygård, A. Geresdi, and M. H. Devoret, Direct Microwave Measurement of Andreev-Bound-State Dynamics in a Semiconductor-Nanowire Josephson Junction, *Phys. Rev. Lett.* **121**, 047001 (2018).
- [46] A. Bargerbos, W. Uilhoorn, C.-K. Yang, P. Krogstrup, L. P. Kouwenhoven, G. de Lange, B. van Heck, and A. Kou, Observation of Vanishing Charge Dispersion of a Nearly Open Superconducting Island, *Phys. Rev. Lett.* **124**, 246802 (2020).
- [47] A. Kringsøj, B. van Heck, T. W. Larsen, O. Erlandsson, D. Sabonis, P. Krogstrup, L. Casparis, K. D. Petersson, and C. M. Marcus, Suppressed Charge Dispersion via Resonant Tunneling in a Single-Channel Transmon, *Phys. Rev. Lett.* **124**, 246803 (2020).
- [48] W. Uilhoorn, J. G. Kroll, A. Bargerbos, S. D. Nabi, C.-K. Yang, P. Krogstrup, L. P. Kouwenhoven, A. Kou, and G. de Lange, Quasiparticle trapping by orbital effect in a hybrid superconducting-semiconducting circuit, arXiv e-prints (2021), ArXiv:2105.11038.
- [49] F. J. M. Cañadas, C. Metzger, S. Park, L. Tosi, P. Krogstrup, J. Nygård, M. F. Goffman, C. Urbina, H. Pothier, and A. Levy Yeyati, Signatures of interactions in the Andreev spectrum of nanowire Josephson junctions (2021), ArXiv:2112.05625.
- [50] P. D. Kurilovich, V. D. Kurilovich, V. Fatemi, M. H. Devoret, and L. I. Glazman, Microwave response of an Andreev bound state, *Phys. Rev. B* **104**, 174517 (2021).
- [51] C. Hermansen, A. Levy Yeyati, and J. Paaske, Inductive microwave response of Yu-Shiba-Rusinov states, *Phys. Rev. B* **105**, 054503 (2022).
- [52] V. Fatemi, P. D. Kurilovich, M. Hays, D. Bouman, T. Connolly, S. Diamond, N. E. Frattini, V. D. Kurilovich, P. Krogstrup, J. Nygård, A. Geresdi, L. I. Glazman, and M. H. Devoret, Microwave susceptibility observation of interacting many-body Andreev states, arXiv e-prints (2021), ArXiv:2112.05624.
- [53] B. I. Spivak and S. A. Kivelson, Negative local superfluid densities: The difference between dirty superconductors and dirty Bose liquids, *Phys. Rev. B* **43**, 3740 (1991).
- [54] A. Blais, R.-S. Huang, A. Wallraff, S. M. Girvin, and R. J. Schoelkopf, Cavity quantum electrodynamics for superconducting electrical circuits: An architecture for quantum computation, *Phys. Rev. A* **69**, 062320 (2004).
- [55] K. G. Wilson, The renormalization group: Critical phenomena and the Kondo problem, *Rev. Mod. Phys.* **47**, 773 (1975).

- [56] K. Satori, H. Shiba, O. Sakai, and Y. Shimizu, Numerical renormalization group study of magnetic impurities in superconductors, *J. Phys. Soc. Jpn.* **61**, 3239 (1992).
- [57] R. Bulla, T. A. Costi, and T. Pruschke, The numerical renormalization group method for quantum impurity systems, *Rev. Mod. Phys.* **80**, 395 (2008).
- [58] P. Krogstrup, N. L. B. Ziino, W. Chang, S. M. Albrecht, M. H. Madsen, E. Johnson, J. Nygård, C. Marcus, and T. S. Jespersen, Epitaxy of semiconductor-superconductor nanowires, *Nat. Mater.* **14**, 400 (2015).
- [59] J. Koch, T. M. Yu, J. Gambetta, A. A. Houck, D. I. Schuster, J. Majer, A. Blais, M. H. Devoret, S. M. Girvin, and R. J. Schoelkopf, Charge-insensitive qubit design derived from the Cooper pair box, *Phys. Rev. A* **76**, 042319 (2007).
- [60] See the Supplemental Material at <http://link.aps.org/supplemental/10.1103/PRXQuantum.3.030311> for further details about theoretical modeling, device fabrication, experimental setup, device tune-up, analysis for in-field data, and processing of time-domain data, as well as the power, tunnel gate, and temperature dependence of the parity lifetimes. It includes Refs. [94–107].
- [61] M. L. Della Rocca, M. Chauvin, B. Huard, H. Pothier, D. Esteve, and C. Urbina, Measurement of the Current-Phase Relation of Superconducting Atomic Contacts, *Phys. Rev. Lett.* **99**, 127005 (2007).
- [62] A. Blais, A. L. Grimsom, S. M. Girvin, and A. Wallraff, Circuit quantum electrodynamics, *Rev. Mod. Phys.* **93**, 025005 (2021).
- [63] F. Luthi, T. Stavenga, O. W. Enzing, A. Bruno, C. Dickel, N. K. Langford, M. A. Rol, T. S. Jespersen, J. Nygård, P. Krogstrup, and L. DiCarlo, Evolution of Nanowire Transmon Qubits and Their Coherence in a Magnetic Field, *Phys. Rev. Lett.* **120**, 100502 (2018).
- [64] J. G. Kroll, F. Borsoi, K. L. van der Enden, W. Uilhoorn, D. de Jong, M. Quintero-Pérez, D. J. van Woerkom, A. Bruno, S. R. Plissard, D. Car, E. P. A. M. Bakkers, M. C. Cassidy, and L. P. Kouwenhoven, Magnetic-Field-Resilient Superconducting Coplanar-Waveguide Resonators for Hybrid Circuit Quantum Electrodynamics Experiments, *Phys. Rev. Appl.* **11**, 064053 (2019).
- [65] M. Pita-Vidal, A. Bargerbos, C.-K. Yang, D. J. van Woerkom, W. Pfaff, N. Haider, P. Krogstrup, L. P. Kouwenhoven, G. de Lange, and A. Kou, Gate-Tunable Field-Compatible Fluxonium, *Phys. Rev. Appl.* **14**, 064038 (2020).
- [66] N. Samkharadze, A. Bruno, P. Scarlino, G. Zheng, D. P. DiVincenzo, L. DiCarlo, and L. M. K. Vandersypen, High-Kinetic-Inductance Superconducting Nanowire Resonators for Circuit QED in a Magnetic Field, *Phys. Rev. Appl.* **5**, 044004 (2016).
- [67] R. Žitko and T. Pruschke, Energy resolution and discretization artefacts in the numerical renormalization group, *Phys. Rev. B* **79**, 085106 (2009).
- [68] R. Žitko, NRG Ljubljana (2021).
- [69] Note that the notion of singlet and doublet sectors, introduced for the isolated quantum dot, extends naturally to the coupled quantum dot, provided that the spin  $S$  is now regarded as the total spin of the system, including that of quasiparticles in the reservoirs.
- [70] A. Keselman, C. Murthy, B. van Heck, and B. Bauer, Spectral response of Josephson junctions with low-energy quasiparticles, *SciPost Phys.* **7**, 50 (2019).
- [71] J. Ávila, E. Prada, P. San-Jose, and R. Aguado, Superconducting islands with topological Josephson junctions based on semiconductor nanowires, *Phys. Rev. B* **102**, 094518 (2020).
- [72] J. Ávila, E. Prada, P. San-Jose, and R. Aguado, Majorana oscillations and parity crossings in semiconductor nanowire-based transmon qubits, *Phys. Rev. Res.* **2**, 033493 (2020).
- [73] Our assumption that regimes with 0-junction and  $\pi$ -junction behavior correspond to the quantum-dot junction being in a singlet or doublet state, respectively, is only valid in the single-level regime, where the level spacing of the quantum dot is significantly larger than  $\Delta$  and  $U$ . In the multilevel regime, where excited states of the quantum dot are involved, the presence or absence of the  $\pi$  offset also depends on the character of the orbital wave functions in addition to the fermion parity [20].
- [74] G. Kiršanskas, M. Goldstein, K. Flensberg, L. I. Glazman, and J. Paaske, Yu-Shiba-Rusinov states in phase-biased superconductor–quantum dot–superconductor junctions, *Phys. Rev. B* **92**, 235422 (2015).
- [75] A. Kadlecová, M. Žonda, and T. Novotný, Quantum dot attached to superconducting leads: Relation between symmetric and asymmetric coupling, *Phys. Rev. B* **95**, 195114 (2017).
- [76] P. Zalom, V. Pokorný, and T. c. v. Novotný, Spectral and transport properties of a half-filled Anderson impurity coupled to phase-biased superconducting and metallic leads, *Phys. Rev. B* **103**, 035419 (2021).
- [77] S. D. Escribano, A. Levy Yeyati, R. Aguado, E. Prada, and P. San-Jose, Fluxoid-induced pairing suppression and near-zero modes in quantum dots coupled to full-shell nanowires, *Phys. Rev. B* **105**, 045418 (2022).
- [78] R. Žitko and M. Fabrizio, Non-Fermi-liquid behavior in quantum impurity models with superconducting channels, *Phys. Rev. B* **95**, 085121 (2017).
- [79] K. Serniak, S. Diamond, M. Hays, V. Fatemi, S. Shankar, L. Frunzio, R. J. Schoelkopf, and M. H. Devoret, Direct Dispersive Monitoring of Charge Parity in Offset-Charge-Sensitive Transmons, *Phys. Rev. Appl.* **12**, 014052 (2019).
- [80] J. J. Wesdorp, L. Grünhaupt, A. Vaartjes, M. Pita-Vidal, A. Bargerbos, L. J. Splitthoff, P. Krogstrup, B. van Heck, and G. de Lange, Dynamical polarization of the fermion parity in a nanowire Josephson junction, arXiv e-prints (2021), [ArXiv:2112.01936](https://arxiv.org/abs/2112.01936).
- [81] J. Heinsoo, C. K. Andersen, A. Remm, S. Krinner, T. Walter, Y. Salathé, S. Gasparinetti, J.-C. Besse, A. Potočnik, A. Wallraff, and C. Eichler, Rapid High-Fidelity Multiplexed Readout of Superconducting Qubits, *Phys. Rev. Appl.* **10**, 034040 (2018).
- [82] L. I. Glazman and G. Catelani, Bogoliubov quasiparticles in superconducting qubits, *SciPost Phys. Lect. Notes*, 312021.
- [83] K. Serniak, M. Hays, G. de Lange, S. Diamond, S. Shankar, L. D. Burkhardt, L. Frunzio, M. Houzet, and M. H. Devoret, Hot Nonequilibrium Quasiparticles in Transmon Qubits, *Phys. Rev. Lett.* **121**, 157701 (2018).

- [84] T. W. Larsen, M. E. Gershenson, L. Casparis, A. Kringhøj, N. J. Pearson, R. P. G. McNeil, F. Kuemmeth, P. Krogstrup, K. D. Petersson, and C. M. Marcus, Parity-Protected Superconductor-Semiconductor Qubit, *Phys. Rev. Lett.* **125**, 056801 (2020).
- [85] J. D. Sau and S. D. Sarma, Realizing a robust practical Majorana chain in a quantum-dot-superconductor linear array, *Nat. Commun.* **3**, 1 (2012).
- [86] I. C. Fulga, A. Haim, A. R. Akhmerov, and Y. Oreg, Adaptive tuning of Majorana fermions in a quantum dot chain, *New J. Phys.* **15**, 045020 (2013).
- [87] J. P. T. Stenger, B. D. Woods, S. M. Frolov, and T. D. Stanescu, Control and detection of Majorana bound states in quantum dot arrays, *Phys. Rev. B* **98**, 085407 (2018).
- [88] I. M. Dayton, T. Sage, E. C. Gingrich, M. G. Loving, T. F. Ambrose, N. P. Siwak, S. Keebaugh, C. Kirby, D. L. Miller, A. Y. Herr, Q. P. Herr, and O. Naaman, Experimental demonstration of a Josephson magnetic memory cell with a programmable  $\pi$ -junction, *IEEE Magn. Lett.* **9**, 1 (2018).
- [89] E. Ginossar and E. Grosfeld, Microwave transitions as a signature of coherent parity mixing effects in the Majorana-transmon qubit, *Nat. Commun.* **5**, 1 (2014).
- [90] D. I. Pikulin, B. van Heck, T. Karzig, E. A. Martinez, B. Nijholt, T. Laeven, G. W. Winkler, J. D. Watson, S. Heedt, M. Temurhan, V. Svidenko, R. M. Lutchyn, M. Thomas, G. de Lange, L. Casparis, and C. Nayak, Protocol to identify a topological superconducting phase in a three-terminal device, arXiv e-prints (2021), [ArXiv:2103.12217](https://arxiv.org/abs/2103.12217).
- [91] S. Ahn, H. Pan, B. Woods, T. D. Stanescu, and S. Das Sarma, Estimating disorder and its adverse effects in semiconductor Majorana nanowires, *Phys. Rev. Mater.* **5**, 124602 (2021).
- [92] J. Schulenborg and K. Flensberg, Absence of supercurrent sign reversal in a topological junction with a quantum dot, *Phys. Rev. B* **101**, 014512 (2020).
- [93] E. Prada, P. San-Jose, M. de Moor, A. Geresdi, E. Lee, J. Klinovaja, D. Loss, J. Nygård, R. Aguado, and L. Kouwenhoven, From Andreev to Majorana bound states in hybrid superconductor-semiconductor nanowires, *Nat. Rev. Phys.* **2**, 575 (2020).
- [94] P. Welch, The use of fast Fourier transform for the estimation of power spectra: A method based on time averaging over short, modified periodograms, *IEEE Trans. Audio Electroacoust.* **15**, 70 (1967).
- [95] H. Krishna-murthy, J. Wilkins, and K. Wilson, Renormalization-group approach to the Anderson model of dilute magnetic alloys. i. Static properties for the symmetric case, *Phys. Rev. B* **21**, 1003 (1980).
- [96] M. D. Schroer, K. D. Petersson, M. Jung, and J. R. Petta, Field Tuning the  $g$  Factor in InAs Nanowire Double Quantum Dots, *Phys. Rev. Lett.* **107**, 176811 (2011).
- [97] I. M. Pop, K. Geerlings, G. Catelani, R. J. Schoelkopf, L. I. Glazman, and M. H. Devoret, Coherent suppression of electromagnetic dissipation due to superconducting quasiparticles, *Nature* **508**, 369 (2014).
- [98] E. M. Spanton, M. Deng, S. Vaitiekėnas, P. Krogstrup, J. Nygård, C. M. Marcus, and K. A. Moler, Current-phase relations of few-mode InAs nanowire Josephson junctions, *Nat. Phys.* **13**, 1177 (2017).
- [99] A. Kringhøj, L. Casparis, M. Hell, T. W. Larsen, F. Kuemmeth, M. Leijnse, K. Flensberg, P. Krogstrup, J. Nygård, K. D. Petersson, and C. M. Marcus, Anharmonicity of a superconducting qubit with a few-mode Josephson junction, *Phys. Rev. B* **97**, 060508(R) (2018).
- [100] A. E. Antipov, A. Bargerbos, G. W. Winkler, B. Bauer, E. Rossi, and R. M. Lutchyn, Effects of Gate-Induced Electric Fields on Semiconductor Majorana Nanowires, *Phys. Rev. X* **8**, 031041 (2018).
- [101] S. Hart, Z. Cui, G. Ménard, M. Deng, A. E. Antipov, R. M. Lutchyn, P. Krogstrup, C. M. Marcus, and K. A. Moler, Current-phase relations of InAs nanowire Josephson junctions: From interacting to multimode regimes, *Phys. Rev. B* **100**, 064523 (2019).
- [102] G. W. Winkler, A. E. Antipov, B. van Heck, A. A. Soluyanov, L. I. Glazman, M. Wimmer, and R. M. Lutchyn, Unified numerical approach to topological semiconductor-superconductor heterostructures, *Phys. Rev. B* **99**, 245408 (2019).
- [103] A. Kringhøj, T. W. Larsen, B. van Heck, D. Sabonis, O. Erlandsson, I. Petkovic, D. I. Pikulin, P. Krogstrup, K. D. Petersson, and C. M. Marcus, Controlled dc Monitoring of a Superconducting Qubit, *Phys. Rev. Lett.* **124**, 056801 (2020).
- [104] D. de Jong, C. G. Prosko, D. M. A. Waardenburg, L. Han, F. K. Malinowski, P. Krogstrup, L. P. Kouwenhoven, J. V. Koski, and W. Pfaff, Rapid Microwave-Only Characterization and Readout of Quantum Dots Using Multiplexed Gigahertz-Frequency Resonators, *Phys. Rev. Appl.* **16**, 014007 (2021).
- [105] J. Wesdorp, L. Grünhaupt, A. Vaartjes, M. Pita-Vidal, A. Bargerbos, L. J. Splitthoff, B. van Heck, and G. de Lange, Andreev spectroscopy of an InAs junction in a magnetic field, In preparation (2022).
- [106] L. J. Splitthoff, A. Bargerbos, L. Grünhaupt, M. Pita-Vidal, J. Wesdorp, Y. Liu, A. Kou, C. K. Andersen, and B. van Heck, Gate-tunable kinetic inductance in proximitized nanowires, arXiv e-prints (2022), [ArXiv:2202.08729](https://arxiv.org/abs/2202.08729).
- [107] R. Zitko, Josephson potentials for single impurity Anderson impurity in a junction between two superconductors (2022).
- [108] See <https://doi.org/10.4121/c.5801744>.